Separation of PP and PS converted waves applied in mining exploration

Raphael Di Carlo Silva dos Santos[1,2], João Carlos Ribeiro Cruz[2].
[1]Universidade Federal do Oeste do Pará
[2]Universidade Federal do Pará

This paper was prepared for presentation during the 16th International Congress of the Brazilian Geophysical Society held in Rio de Janeiro, Brazil, 19-22 August 2019.

Abstract

We apply a new methodology of PP and PS separation based on the estimates of the Finite Offset Common Reflection Surface attributes. Once the attributes are inverted we use them to build a separation filter, which is function of the polarization direction of the wave. The method was applied in the so-called N4WS iron ore body, pertaining to the Mineral Province of Carajás, northern Brazil. The filter separated successfully PP and PS amplitudes from sections of the iron ore and the results obtained were stacked in order to increase the signal-to-noise ratio.

Introduction

The seismic methods are essential in upstream chain of oil and gas industry. However due to the great capacity to deal with deep targets the seismic methods are growing in mining sector. In general, potential field and electromagnetic methods have solved problems as to delineate mineralized zones or investigate shallows depths but the reflection or refraction seismic methods are the only ones to provide a high quality images of mineral deposits in high depths (MALHEMIR et al., 2012). The fact that they have greater penetration with sufficient resolution, compared with other geophysical methods, can complement drilling and exploration surveys.

The application of seismic methods in mining engineering and exploration is extensive. They are applied to investigate siderrite mineralization (SCHMIDT, 1959), to delineate sulphide veins (UROCEVIC et al. ,2000; WONG, 2000; BOHLEN et al. ,2003) and kimberlites (UROCEVIC and EVANS, 1998; UROCEVIC and EVANS, 2000; WHITE and KJARSGAARD, 2012), to study cristaline terrains (NEDIMOVIC and WEST, 2003) and to study mine planning (STUART et al., 2000; WOOD et al., 2012). Additionaly, the application of seismic in mining exploration is often limited to PP amplitudes because converted shear waves are rarely recognized or observed in the seismic data. However, elastic-wave theory and finite-difference modeling predict that basic metal deposits can convert a significant part of the incident seismic energy, producing converted shear waves potentially useful for mining exploration. Examples of application are sulphides imaging (BELLEFLEUR et al., 2004; HARVEY, 2007) and monitoring of mines structures (WUESTEFELD et al., 2011).

In this work we apply the separation of PP and PS-waves through the Finite Offset Common Reflection Surface (FO-CRS) traveltime approximation in an ore modelled data. The target is the NW4S iron ore of the Mineral Province of Carajás (MPC), southeastern Pará state, northern Brazil.

Geological Settings

Serra dos Carajás is a mountain range located at west of Marabá city, Pará state, Brazil, that include mining operations in a huge deposit of high-grade iron ore. The NW4S iron orebody is located in The Mineral Province of Carajás (MPC), situated at Parauapebas city, southeastern Pará state (Figure 1), around Serra dos Carajás. The MPC is inside the Amazonian Craton (ALMEIDA et al., 1976). It is divided in two tectonic domains, the south mesoarchean Rio Maria Granite-Greenstone Belt and the north Itacaúnas Shear Belt. The south one is formed by volcano sedimentary sequences and granite intrusions. The north one has a basement characterized by granulites and gneisses with granite composition (SILVA et al., 1974). The supracrustal rocks are represented by neoarchean volcano sedimentary sequences from Itacaúnas Supergroup (MACAMBIRA and SILVA, 1974). The Supergroup Itacaúnas is characterized by mafic-ultramafic layered intrusions formed by anorogenic granites, peridotites, gabbros and pyroxenites. Superimposed to older rocks there are fluvial and marines sequences. The Carajás formation contains iron-banded formation, known as jaspilites, where processes transformed the rock composition generating shallow iron ore bodies. This formation is located in plateaus supported by laterite layers, and it represents the protominerals of the iron deposits of the MPC (MACAMBIRA and SILVA, 1974).

In study area the iron mineral occurrence is in great part a friable hematite, found in depths until 350m and contaminated with aluminum, phosphorous and manganese. Nogueira (2014) performed the acquisition, processing and interpretation of electrorresistivity and refractive seismic 2D data in one profile at N4WS body. The seismic and electrorresistivity lines are, respectively, 1190m and 1470m long, and the

refraction line started at the coordinate 270m of the electric line (Figure 2). Along the profile well logging data were acquired with depths varying between 100m and 550m. Also Nogueira (2014) created a geophysical model and compared it with the available a priori well logging data of the survey area (Figure 2). Holanda (2017) created a P-velocity model from Figure 2 based on a priori geological information of the study area (Figure 3).

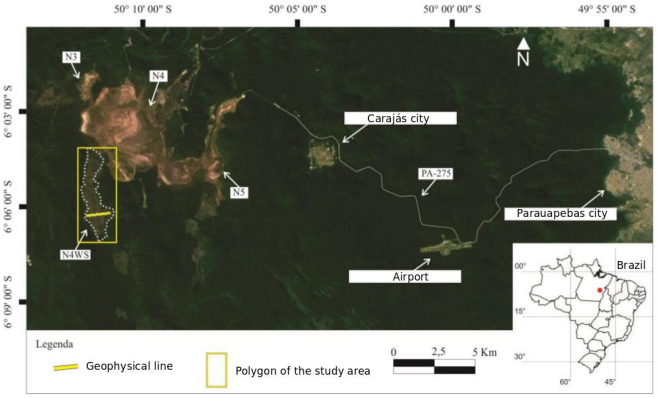

Figure 1 - Location of the N4WS orebody at Mineral Province of Carajás.

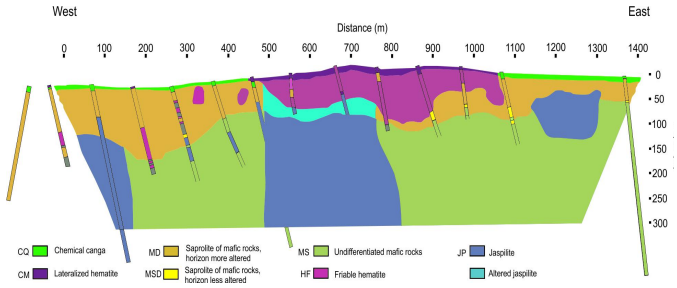

Figure 2 - Geophysical model from the N4WS ore body profile. Adapted from Nogueira (2014).

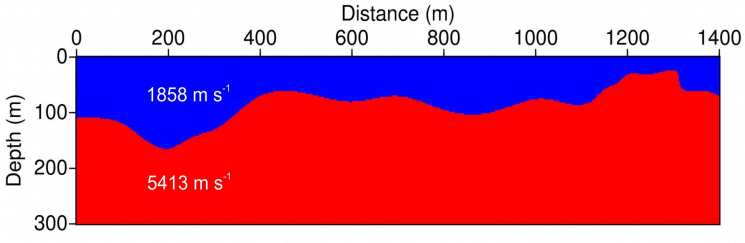

Figure 3 - P-velocity model from Figure 2. Adapted from Holanda (2017).

Finite Offset Common Reflection Surface Traveltime Approximation

Zhang et al. (2001) developed a hyperbolic traveltime approximation for paraxial rays in the vicinity of a central ray considering a finite offset between source and receiver. Making the assumption of a central ray starting from S, reflecting at the subsurface, and emerging at G (Fig.4), the traveltime of the finite offset paraxial ray is

$$
\begin{aligned}
t^2(\Delta x_m,\Delta h)=&\left[t_0+\left(\frac{\sin\beta_G}{v_G}+\frac{\sin\beta_S}{v_S}\right)\Delta x_m+\left(\frac{\sin\beta_G}{v_G}-\frac{\sin\beta_S}{v_S}\right)\Delta h\right]^2\\
&+t_0\left[(4K_1-3K_3)\frac{\cos^2\beta_G}{v_G}-K_2\frac{\cos^2\beta_G}{v_G}\right]\Delta x_m\\
&+t_0\left[K_3\frac{\cos^2\beta_G}{v_G}-K_2\frac{\cos^2\beta_S}{v_S}\right]\Delta h\\
&+2t_0\left[K_3\frac{\cos^2\beta_G}{v_G}+K_2\frac{\cos^2\beta_S}{v_S}\right]\Delta x_m\Delta h.
\end{aligned}
\qquad (1)
$$

The equation (1) is denoted by Finite Offset Common Reflection Surface (FO-CRS) traveltime approximation. The time t_0 is the traveltime along the central ray, β_S and β_G are the start and emergence angles, respectively, of the central ray at the position S with coordinate xS and at the position G with coordinate xG. The displacements $\Delta x_m=x_m-x_0$ and $\Delta h=h-h_0$ correspond to the midpoint and half-offset, respectively, in which $x_0=(xG+xS)/2$ is the midpoint and $h_0=(xG-xS)/2$ is the half-offset of the central ray. The midpoint x_m and the half-offset h are the measured coordinates of a paraxial ray with finite offset. The velocity of the wave at the source and at the receiver are denoted by v_S and v_G , respectively, and we admit $v_S=v_G=v_0$. The parameters K_1 , K_2 and K_3 are the curvatures of the wavefront associated to the central ray computed in the earth surface. Inserting the condition $\Delta x_m=\Delta h$, for which the sources of the paraxial and central ray coincide, the eq. (1) applies

$$
t^2(\Delta h)=\left[t_0+2\left(\frac{\sin\beta_G}{v_G}\right)\Delta h\right]^2+4t_0\left[K_1\frac{\cos^2\beta_G}{v_G}\right]\Delta h^2. \qquad (2)
$$

The equation (2) is the FO-CRS approximation for common shot sections. We refer it as the Common Shot Common Reflection Surface (CS-CRS) traveltime approximation. In other hand if we insert the condition $\Delta x_m=0$ in eq. (1) it applies

$$t^2(\Delta h)=\left[t_0+\left(\frac{\sin\beta_G}{v_G}-\frac{\sin\beta_S}{v_S}\right)\Delta h\right]^2$$
$$+t_0\left[K_3\frac{\cos^2\beta_G}{v_G}-K_2\frac{\cos^2\beta_S}{v_S}\right]\Delta h^2. \quad (3)$$

The equation (3) is the FO-CRS approximation for common shot sections and it is referred as Common Midpoint Common Reflection Surface (CMP-CRS) traveltime approximation.

We use the inversion of the parameters (K_1,K_2, K_3,β_G, β_S) to perform the wave separation and to stack the separated section using the curves derived from FO-CRS.

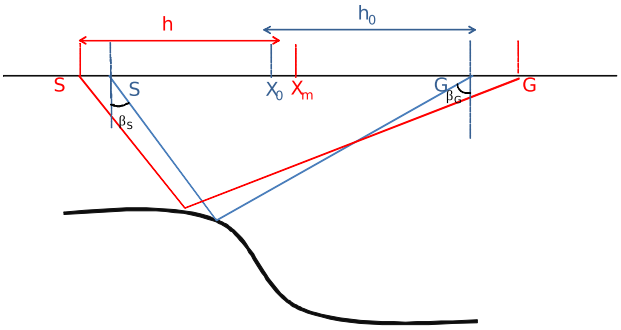

Figure 4 - Diagram of a paraxial ray (red) at the vicinity of a central ray (blue) traveling from a source S to a receiver G in a smooth medium.

Separation Filter

We use the separation factor developed by Bergler et al. (2002) to create a new separation filter. In principle the PP- and PS-separation method does not take into account the existence of multiple reflections, refracted waves, ground roll or direct waves, so it works only on data with primary reflections. Assume the angles β_S and β_G from CRS approximations, they define, respectively, the direction of the central ray at the source and at the receiver in respect to a vertical axis. According to the type of emerging wave, the angle β_G must coincide with the direction of polarization angle, calculated directly from the vertical component of the seismic section. If a P-wave ray reaches the receiver, the direction of polarization and the angle β_G coincides, in other hand if a S-wave ray reaches the receiver the direction of polarization angle and β_G are different.

The methodology uses a criterion separation to extract PP and PS amplitudes isolatedly: the difference angle denoted by γ, between the directly measured angle polarization of P- or S-waves, ψ and the angle of emerging ray, β_G . If ψ and β_G coincides, the conditions $\gamma \approx 0$ applies, otherwise $\gamma \neq 0$. Then a weight factor $w(\gamma)$ is required to suppress events with large γ and to preserve events with γ near zero. We modified the factor given by Bergler et al. (2002) in the form of

$$w_p(\gamma)=\left|\cos^{2n+1}\gamma\right|, n\geq 0, \quad (4)$$
$$w_s(\gamma)=\left|\sin^{2n+1}\gamma\right|, n\geq 0. \quad (5)$$

To extract PP amplitudes we use eq. (4) because P-waves have polarization direction coincident to the ray direction. To extract PS amplitudes we use eq. (5) because S-waves polarization and the ray directions are approximately perpendicular, so amplitudes with $\gamma \approx 0$ are attenuated.

After the separation we stack the separated sections in order to increase the signal-to-noise ratio. The stacking is performed using the CS-CRS curve in common shot sections or CMP-CRS curve in common offset sections. The curves parameters are estimated using the Very fast Simulated annealing optimization algorithm (SEN & STOFFA, 2013).

Results

We used a profile with 1400m in extension with 241 receivers spaced 5m each in split-spread common shot geometry. The source wavelet is the Fuchs-Mueller signal

$$s(\Delta t)=4\pi\Delta k^2\left[\sin\left(\frac{2\pi j\Delta t}{\varepsilon}\right)-\frac{1}{2}\sin\left(\frac{4\pi j\Delta t}{\varepsilon}\right)\right], \quad (6)$$

where Δt is the time sampling interval, j is the time sampling index, Δk is the space sampling interval and ε is the signal time duration.

The data was generated through the discretization of the wave equation for a second order operator in a generalized elastic medium using a conventional standard staggered-grid. We use the values Δ t = 0.0002029s, Δ k=0.00025km, ε =0.0125s and peak frequency of 80Hz. All data were modelled using the package SOFI2D (Bohlen et al., 2015).

The Figure 5 shows the vertical component section of one shot, with the source located at 0.75km, with PP (red curve) and PS amplitudes (blue curve). The Figure 6 shows the separation with PS amplitudes attenuated and Figure 7 show the separation with PP amplitudes attenuated. For both cases we used the filter with order n = 1. In order to quantify the amplitudes attenuation and the efficiency of the separation filter, we subtracted the filtered sections with the original one.

The Figure 8 and 9 show, respectively, the difference between the Figure 6 and 7 with Figure 5. In the Figure 8 the events associated to PS amplitudes tend to high values due to the high attenuation. The difference between the filtered amplitude and the original one is high such that the attenuation is high . In yellow and light blue zones of the PS reflection the difference is almost 5 times lesser than the original PS amplitude, then

the attenuation holds an order of 2 to 5. In the same way the PP attenuation holds an order of 0.5 to 1.5. In the same way at Figure 9 the PP events represent a difference of 1.5 to 2.2 times from the original section, while the PS events represent a difference of 0.2 to 0.6 the original section. It means the filter almost did not attenuate PS reflections and attenuated great part of the PP reflections, as intended as well.

The Figure 10 and 11 show the respective vertical and horizontal component of common offset section with offset 0.23km with PP and PS amplitudes. The Figure 12 shows the separation with PP amplitudes extracted in the vertical component section and Figure 13 shows the separation with PS amplitudes extracted in the same vertical component section. The power filter used was n=0 for all separation. The Figure 14 shows the difference between Figure 12 and Figure 10 and the Figure 15 shows the difference between Figure 13 and 10. In yellow and light blue zones of the PS reflection the difference order of the amplitudes are 0.3 to 2 times lesser than the original PS reflection. The attenuation of the PP reflections has an order of 0.5 to 2 times. The amplitude differences showed that there were no great loss of information in the separation of PP or PS amplitudes.

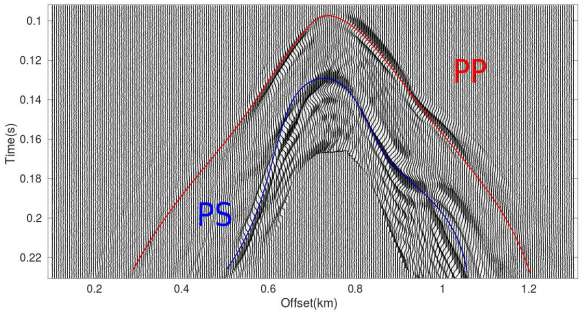

Figure 5 - Common shot section from the N4WS orebody profile. Red curve indicates PP reflection and blue curve indicate PS reflection.

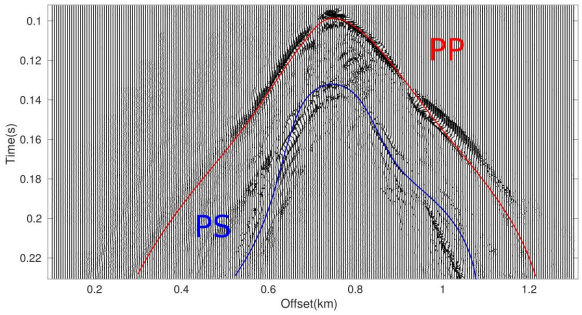

Figure 6 - CS-CRS stacked section with PS reflections attenuated and PP reflections extracted.

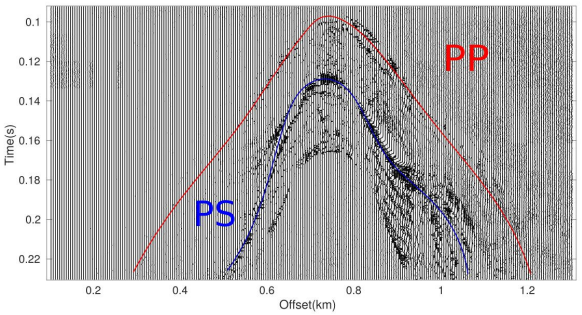

Figure 7 - CS-CRS stacked section with PP reflections attenuated and PS reflections extracted.

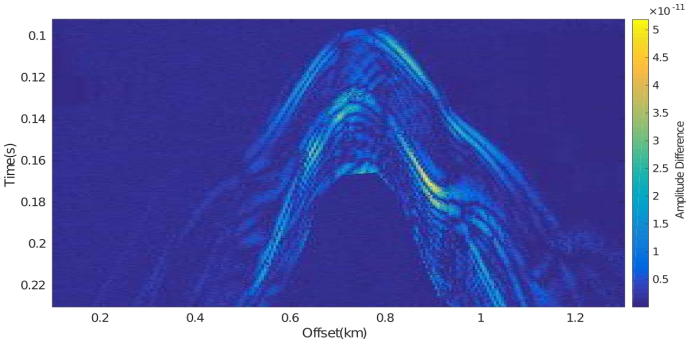

Figure 8 - Amplitude difference between Figure 6 and Figure 5.

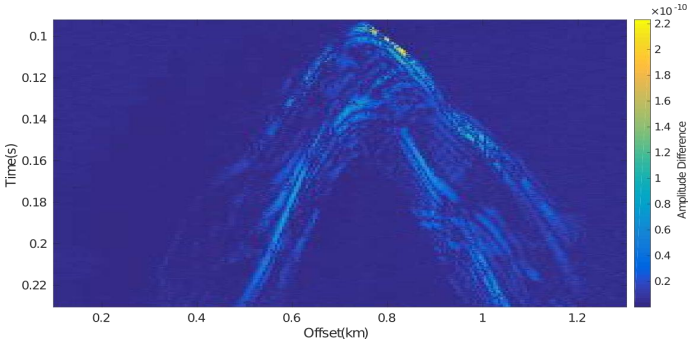

Figure 9 - Amplitude difference between Figure 7 and Figure 5.

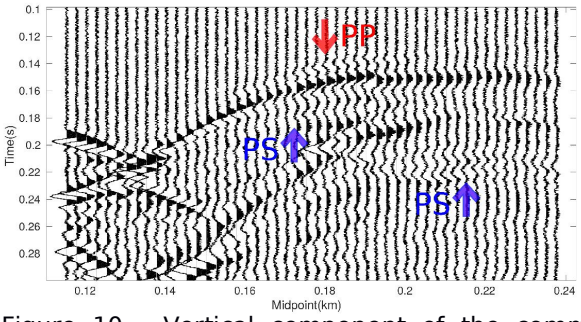

Figure 10 - Vertical component of the common offset section 0.23km from the N4WS orebody profile. Red curve indicates PP reflection and blue curve indicate PS reflection.

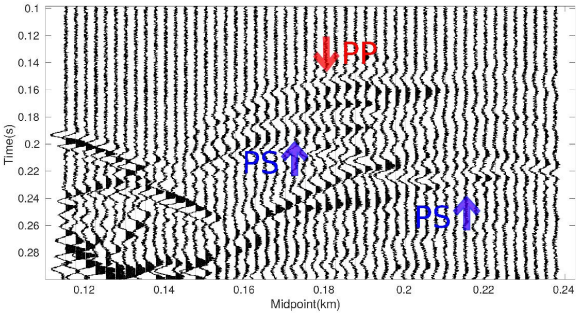

Figure 11 - Horizontal component of the common offset section 0.23km from the N4WS orebody profile. Red curve indicates PP reflection and blue curve indicate PS reflection.

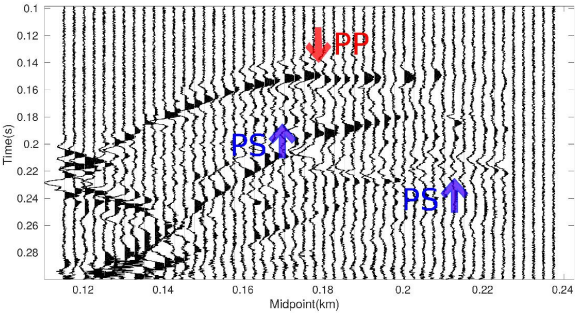

Figure 12 - CMP-CRS stacked CO section with PP reflections extracted.

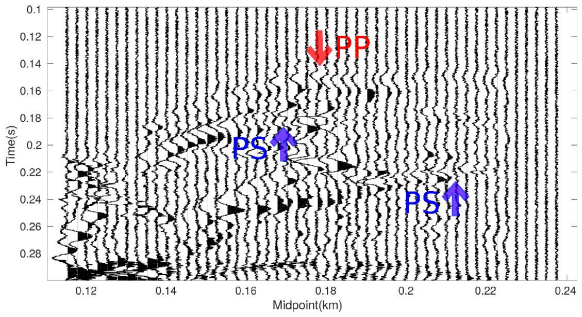

Figure 13 - CMP-CRS stacked CO section with PS reflections extracted.

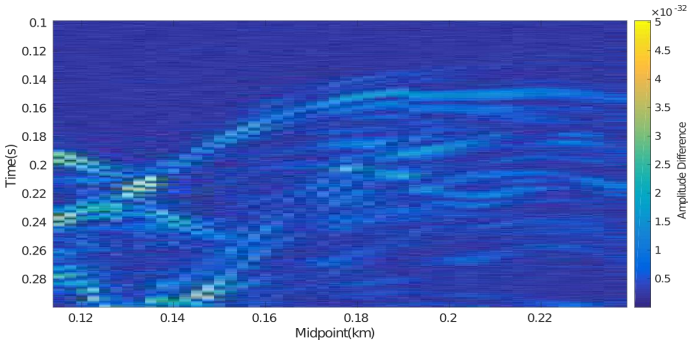

Figure 14 - Amplitude difference between the Figure 12 and Figure 10.

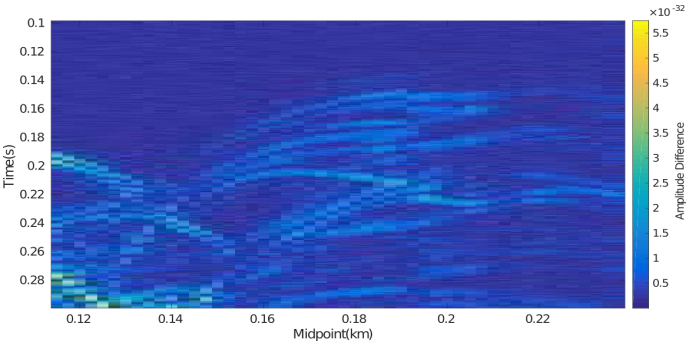

Figure 15 - Amplitude difference between the Figure 13 and Figure 10.

Conclusions

We demonstrated the applicability of a PP- and PS-wave separation filter in seismic multi-coverage data containing converted reflections. This approach is based on the inversion of the CRS traveltime approximation parameters to separate PP- and PS-reflections. After the inversion estimates, we used one parameter as input of a separation filter to extract separatedely PP and PS amplitudes in vertical component sections. Then we use the other parameters to stack the separated sections based on the curves derived from FO-CRS.

The results of the geophysical model from N4WS orebody showed a good separation even in a zone with synclinal structure. As perspectives for future works, we recommend the use of different inversion algorithms to estimate the FO-CRS parameters in order to investigate the numerical accuracy of the results. Also it is important to investigate the possibilities to treat with the conflicting dip problem.

Acknowledgments

The authors thank PETROBRAS for supporting the computational infrastructure of the Seismic Wave Inversion Lab of the Federal University of Pará

(UFPA) and Rafael Holanda for sharing the velocity model used in this work.

References

Almeida, F., Y. Hasui, and B. Brito Neves, 1976, The upper Precambrian of South America: Boletim do Instituto de Geociências, 7, 45–80.

Bellefleur, C., C. Müller, D. Snyder, and L. Matthews, 2004, Downhole seismic imaging of a massive sulfide orebody with mode-converted waves, Halfmile Lake, New Brunswick, Canada: Geophysics, 69, 318–329.

Bergler, S., E. Duveneck, G. Hoecth, Y. Zhang, and P. Hubral, 2002, Common-reflection-surface stack for converted waves: Studia Geophysica et Geodaetica, 165–175.

Bohlen, T., C. Müller, , and B. Milkereit, 2003, Elastic wave scattering from massive sulfide orebodies: On the role of composition and shape: Hardrock seismic exploration: Society of Exploration Geophysicists, 70–83.

Bohlen, T., D. De Nil, D. Köhn, and S. Jetschny, 2015, SOFI2D - seismic modelling with finite differences 2D - elastic and viscoelastic version. User Guide: Karlsruher Institut für Technologie.

Holanda, R., 2017, Modelagem símica acústica por diferenças finitas e imageamento do depósito de minéio de ferro N4WS no Estado do Pará: Master's dissertation, Universidade Federal do Pará.

Macambira, M., and V. Silva, 1974, Estudo petrológico, Mineralógico e Caracterização dasEstruturas Sedimentares e Diagenéticas Preservadas na Formação Carajás: Technical report, Museu Paraense Emílio Goeldi.

Nedimovic, M., and G. West, 2003, Crooked-line 2D seismic reflection imaging in crystallineterrains: Part 1, Data processing: Geophysics, 68, 274–285.

Nogueira, P., 2014, Integração de sísmica de refração e eletrorresistividade para elaboração de um modelo 2D do depósito de ferro N4WS do complexo Serra Norte, Carajás-PA: Master's dissertation, Universidade de Brasília.

Schmidt, G., 1959, Results of underground seismic reflection investigations in siderite district of the Siegerland: Journal of Geophysical Prospecting, 287–290.

Sen, K., and P. Stoffa, 2013, Global optimization methods in geophysical inversion: Cambridge University Press.

Silva, G., M. Lima, A. Andrade, R. Issler, and G. Guimarães, 1974, Levantamentos de recursos naturais, geologia, folhas SB 22 araguaia e parte SC 22 tocantins: Technicalreport, Projeto RADAM Brasil.

Stuart, G. W., S. J. Jolley, L. G. B. T. Palome, and R. F. Tcuker, 2000, Application of 3-D seismic attributes analysis to mine planning: Target gold deposit, South Africa: The Leading Edge, 736–742.

Urocevic, M., and B. Evans, 1998, Seismic methods for the detection of kimberlite pipes:Exploration Geophysics, 29, 632–635.

White, D., and B. Kjarsgaard, 2012, Seismic delineation of the Orion South kimberlite, Fort à la Corne: Geophysics, 77.

Wong, J., 2000, Crosshole seismic imaging of sulphide orebody delineation near Sudbury,Ontario, Canada: Geophysics, 65, 1900–1907.

Wood, G., C. O'Dowd, C. Cosma, , and N. Enescu, 2012, An interpretation of surface and borehole seismic surveys for mine planning at the Millennium uranium deposit, northern Saskatchewan, Canada: Geophysics, WC203–WC212.

Wuestefeld, A., J. Kendall, J. Verdon, and A. Van As, 2011, In situ monitoring of rock fracturing using shear wave splitting analysis: an example from a mining setting: Geophysical Journal International, 187, 848–860.

Zhang, Y., S. Bergler, and P. Hubral, 2001, Common-reflection-surface (CRS) stack for common offset: Geophysical Prospecting, 49, 709–718.